

Spatial Focusing of Surface Polaritons Based on Cross-Phase Modulation

Chaohua Tan^{1,a}, Na Li¹, Datang Xu², Zhiming Chen³ and Yong Zhou¹

¹*School of Physics and Electronics,*

Shandong Normal University, Jinan 250014, China

²*School of Electronic and Information Engineering,*

Changshu Institute of Technology, Changshu 215500, China

³*School of Science, East China University of Technology, Nanchang 330013, Jiangxi, China*

(Dated: October 10, 2021)

Abstract

We theoretically study the spatial focusing of surface polaritons (SPs) in a negative index metamaterial (NIMM)-atomic gas interface waveguide system, based on cross phase modulation (XPM) in a tripod type double electromagnetically induced transparency (EIT) scheme. In the linear region, we realize the low loss stable propagation of SPs, and the group velocities of the probe and signal fields are well matched via double EIT. In the nonlinear region, we show that giant enhancement of the XPM can be obtained. Using a narrow optical soliton in free space, we realize spatial focusing of the SPs solitons, including bright, multi bright, and dark solitons. The full width at the half-maximum (FWHM) of the SPs soliton can be compressed to about ten nanometers, thus, even nanofocusing can be obtained. The results obtained here have certain theoretical significance for nano-scale sensing, spectral enhancement and precision measurement.

^a tanch@sdnu.edu.cn

I. INTRODUCTION

Spatial focusing of surface plasmon polaritons (SPPs), especially at nanoscale, recently has been one of the hot spots in the field of micro-nano optics due to its huge application potentials [1]. It not only provides a powerful technical basis for the development of nano optical devices, but also extends the research realm of strong field micro-nano optics [2], such as near-field and super-resolution imaging [3–13], biological sensing [14, 15], enhanced Raman spectroscopy [16–22], nonlinear spectroscopy [23–25] and photofield electron emission [26], *etc.*

In 2004, Stockman proposed that SPPs nano-focusing refers to the phenomenon that when SPs propagate along the tapered metallic nanostructure, the propagation energy is highly concentrated at the tip of the tapered structure [2]. In recent studies, it is mentioned that tapered nanoribbons and metallic tips can be used to construct nano-focusing waveguides by means of micro-nano manufacturing, and have been applied in many fields [27–31]. For examples, in 2012, Choo *et al.* achieved efficient nano-focusing of SPPs experimentally, which can focus light to a few nanometers with low loss [29]; Zenin *et al.* used the tapered nanoribbon structure to detect that the light field energy can be concentrated in a space of tens of nanometers through nanofocusing, and the near field intensity at the tip of the tapered waveguide can be enhanced to the order of thousands in 2015 [30]; Zhu *et al.* realized SPPs nano-focusing at the tip of the round tower structure, which enhanced the electric field at the tip of the round tower and obtained nano-level light spots in 2019 [10]. SPPs nano-focusing can also be used as an alternative method to prepare nano-light sources for optical nanoimaging [12, 13]. For example, in 2020, Umakoshi *et al.* used nano-focusing of SPPs on tapered metallic nanostructures with a tip diameter of tens of nanometers to obtain a white nano light source in the entire visible light wavelength range [12].

However, metallic nano structures adopted in the above research are all based on high precision micro/nano manufacturing technology, once the structures is prepared, the performance of the device is almost determined, and it is lack of active control. In this work, we propose an active approach to achieve spatial focusing of surface polaritons (SPs, which is excited at the surface of negative index metamaterials and can propagate with low loss for a long distance [32–35]) based on cross-phase modulation (XPM). Actually, the research of compressing pulses in time domain or frequency domain via XPM in fiber optics is very

mature [36–39], the physical mechanism is based on the competitive interaction between dispersion and nonlinearity. Thus, we can also use the competitive interaction between diffraction and nonlinearity to realized the spatial focusing of SPs. Such expansion is like the relation between temporal soliton and spatial soliton [40].

In this article, we propose a general theoretical scheme to investigate spatial focusing of SPs in a negative index metamaterial (NIMM)-atomic gas interface waveguide, based on XPM in a tripod type double electromagnetically induced transparency (EIT) system. First, we obtain the low loss stable propagation of SPs, and the group velocities of the probe and signal fields are well matched under the double EIT condition in the linear region, and then, giant enhancement of the XPM can be obtained in the nonlinear region. Finally, the coupled NLSEs are derived in our system, by adopting the bright-bright soliton pair, multi bright solitons pairs and dark-dark soliton pair solution as the initial condition, we realize the spatial focusing of SPs solitons via XPM between the narrow optical soliton in free space and the SPs soliton, and even nanofocusing.

The rest of the paper is organized as follows: In Sec. II, we propose the theoretical model for the study. In Sec. III, the linear and nonlinear properties of the signal and probe fields, together with the nonlinear envelope equations are given. In Sec. IV, spatial focusing of SPs is studied. Finally, in Sec. V, we summarize the main work of this paper.

II. THEORETICAL MODEL

The system under study consists of a layer of NIMM in the lower half plane $z < 0$ and a cold atomic gas in the upper half plane $z > 0$, as shown in Fig.1(a). The permittivity ϵ_1 and permeability μ_1 of the NIMM are given by the Drude model in optical region [32]. The SPs is excited and propagates in the x direction. The probe field which is narrow in the y direction propagates along the surface of the NIMM in the x direction. The control field incidences in the vertical direction.

The cold atomic gas is chosen as a double-EIT excitation medium with a tripod-type four-level configuration. The three fields are interacting with the atoms coherently as shown in Fig.1(b). The weak probe field \mathbf{E}_p with center angular frequency ω_p couples $|1\rangle \leftrightarrow |4\rangle$, the weaker signal field \mathbf{E}_s with center angular frequency ω_s couples the transition $|2\rangle \leftrightarrow |4\rangle$, and the strong control field \mathbf{E}_c with center angular frequency ω_c couples $|3\rangle \leftrightarrow |4\rangle$, Δ_j

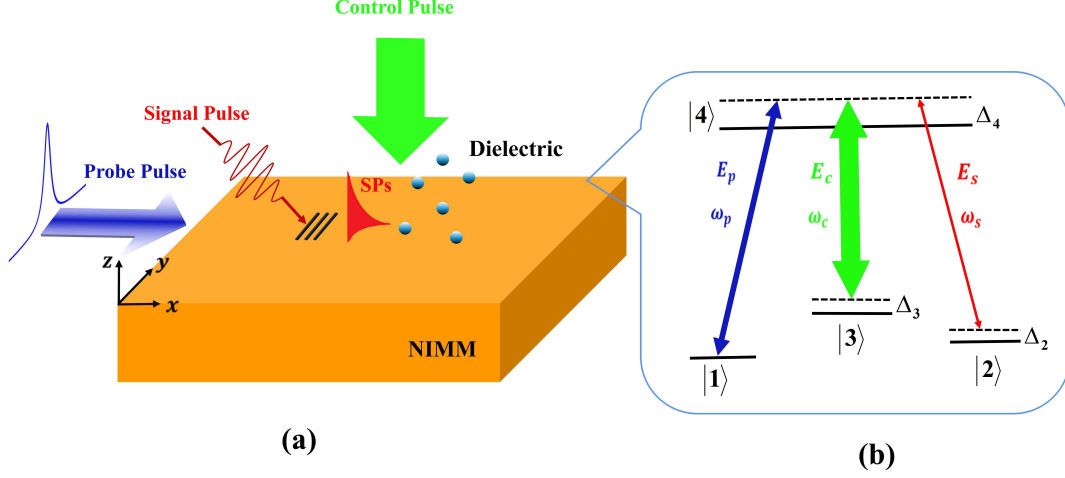


FIG. 1. (Color online) (a) A scheme for nanofocusing of the SPs via XPM. The SPs is excited and propagates in the x direction. The probe field which is narrow in the y direction propagates along the surface of the NIMM in the x direction. The control field incidences in the vertical direction. (b) The cold atomic gas is charged above the surface, and with a tripod-type four-level excitation configuration. The probe, signal and control fields are coupled to the transition $|1\rangle \leftrightarrow |4\rangle$, $|2\rangle \leftrightarrow |4\rangle$ and $|3\rangle \leftrightarrow |4\rangle$, respectively. Δ_j ($j = 2, 3, 4$) are the optical detunings.

($j = 2, 3, 4$) are the optical detunings. The atoms occupying the excited state $|4\rangle$ can spontaneously radiate to the three ground states ($|1\rangle$, $|2\rangle$, and $|3\rangle$) with spontaneous emission rates Γ_{j4} ($j = 1, 2, 3$). The transition between the three ground states are forbidden, but, there may be other dephasing processes, such as collision, we denote such dephasing rates by Γ_{jl} (between the states $|j\rangle$ and $|l\rangle$, $j, l = 1, 2, 3$), those dephasing rates are relatively small comparing with spontaneous emission rates, thus, we assume such processes could not cause the population exchange between the ground states. Such a system can support the propagation of lossless SPs, and provides a great platform for studying the nonlinearity of SPs during interacting with the coherent medium [32].

The signal field is chosen as a TM mode of the waveguide, with the electric field being $\mathbf{E}_s = \mathcal{E}_s \mathbf{u}_s(z) e^{i(k(\omega_s)x - \omega_s t)} + c.c.$, in which, $\mathbf{u}_s(z)$ is the mode function in the z direction [35]. The probe and control fields are chosen as $\mathbf{E}_{c(p)} = \mathcal{E}_{c(p)} \mathbf{e}_{c(p)} e^{i(k_{c(p)}x - \omega_{c(p)}t)} + c.c..$ \mathcal{E}_j ($j = p, s, c$)

represents the envelope of the three fields.

In interaction picture, under the electric-dipole and rotating-wave approximations, the Hamiltonian of the system reads

$$\hat{H}_{int} = -\hbar \sum_{j=1}^4 \Delta_j |j\rangle\langle j| - \hbar [\Omega_c |4\rangle\langle 3| + \Omega_p |4\rangle\langle 1| + \zeta_s(z) \Omega_s e^{i\theta_s} |4\rangle\langle 2| + h.c.], \quad (1)$$

with $\Omega_c = |\mathbf{p}_{34}| \mathcal{E}_c / \hbar$, $\Omega_p = |\mathbf{p}_{14}| \mathcal{E}_p / \hbar$, $\Omega_s = |\mathbf{p}_{24}| \mathcal{E}_s / \hbar$ being the half-Rabi frequencies of the control, probe and signal fields, respectively. $\mathbf{p}_{jl} = p_{jl} \mathbf{e}_{jl}$ is the electric dipole matrix element related to the transition from $|j\rangle$ to $|l\rangle$. $\zeta_s(z) = \mathbf{u}_s(z) \cdot \mathbf{e}_{24}$ is the mode intensity distribution function describing the interaction weight between SPs and atoms along the z firection. $\theta_s = [k(\omega_s) + k_2 - k_4]$ are phase mismatches caused by the eigen dispersion of SPs, where k_l ($l = 2, 4$) refers to the wave number of the state $|l\rangle$.

The interaction information of the system is given by the density matrix σ , which is a 4×4 matrix, and the evolution of σ is governed by the optical Bloch equation [35]

$$\frac{\partial \sigma}{\partial t} = -\frac{i}{\hbar} [\hat{H}_{int}, \sigma] - \Gamma \sigma, \quad (2)$$

with Γ being a 4×4 relaxation matrix which describes the spontaneous emission and other dephasing effects of the system. The detailed expressions of the density matrix σ are given in Appendix B.

Under the condition of slowly varying envelope approximation, the Maxwell equations can be reduced to

$$i\left(\frac{\partial}{\partial x} + \frac{1}{c} \frac{\partial}{\partial t}\right) \Omega_p + \frac{1}{2k_p} \frac{\partial^2}{\partial y^2} \Omega_p + \kappa_{14} \sigma_{41} = 0, \quad (3a)$$

$$i\left(\frac{\partial}{\partial x} + \frac{1}{n_{\text{eff}}} \frac{1}{c} \frac{\partial}{\partial t}\right) \zeta_s(z) e^{i\theta_s} \Omega_s + \frac{1}{2k(\omega_s)} \frac{\partial^2}{\partial y^2} \zeta_s(z) e^{i\theta_s} \Omega_s + \kappa_{24} \sigma_{42} = 0, \quad (3b)$$

where $\kappa_{14} = \mathcal{N}_a \omega_p^2 |\mathbf{p}_{14}|^2 / [2\hbar \varepsilon_0 c^2 \tilde{k}(\omega_p)]$ and $\kappa_{24} = \mathcal{N}_a \omega_s^2 |\mathbf{p}_{24}|^2 / [2\hbar \varepsilon_0 c^2 \tilde{k}(\omega_s)]$ are the coupling coefficients of the probe field and the signal field, $\tilde{k} = \text{Re}(k)$, $n_{\text{eff}} = k(\omega_s) c / \omega_s$ is the effective refractive index, \mathcal{N}_a represents the number density of the atoms, and c is the speed of light in vacuum.

Equations (2) and (3) can totally describe the interaction and propagation properties of our system, which is known as the Maxwell-Bloch (MB) equations. Note that, the Rabi frequencies of the three fields in our system satisfies the condition $|\Omega_s| \ll |\Omega_p| \ll |\Omega_c|$, thus, Eqs. (2) and (3) can be solved by the multi-scale method [41].

III. THE LINEAR AND NONLINEAR PROPERTIES OF THE SYSTEM

Firstly, we make the asymptotic expansion: $\sigma_{jl} - \sigma_{jl}^{(0)} = \epsilon \sigma_{jl}^{(1)} + \epsilon^2 \sigma_{jl}^{(2)} + \dots$, $\Omega_p = \epsilon \Omega_p^{(1)} + \epsilon^2 \Omega_p^{(2)} + \epsilon^3 \Omega_p^{(3)} + \dots$ and $\Omega_s = \epsilon^2 \Omega_s^{(2)} + \epsilon^3 \Omega_s^{(3)} + \dots$, where, ϵ is a dimensionless small parameter characterizing the typical amplitude ratio of the probe field and the signal field, and $\sigma_{jl}^{(0)}$ is the initial state of the system, and all the physical quantities on the right side of the equation are functions of the multiple scales variable $t_j = \epsilon^j t$, $x_j = \epsilon^j x$ ($j = 0, 2$) and $y_1 = \epsilon y$. We can get a series of linear but nonhomogeneous equations about $\sigma_{jl}^{(\alpha)}$, $\Omega_p^{(\alpha)}$, and $\Omega_s^{(\alpha)}$, that can be solved order by order.

A. LINEAR PROPERTIES OF THE SYSTEM

Firstly, we will show that a ultra-low loss propagation of SPs in the linear region, and group velocity matching between the probe and signal fields can be realized via the double EIT effect.

When there is no probe field and signal field, we can obtain the zero-order solution of the system, which corresponding to the initial state of the system, $\sigma_{jl}^{(0)} = 0$, $\sigma_{33}^{(0)} = \sigma_{44}^{(0)} = 0$, $\sigma_{11}^{(0)} + \sigma_{22}^{(0)} = 1$. Thus, there are no coherence between the states, and all atoms populate on the ground states $|1\rangle$ and $|2\rangle$. For convenience, we have assumed that $\sigma_{11}^{(0)} = \sigma_{22}^{(0)} = 1/2$ in the following discussions, which means atoms is uniformly distributed in the states $|1\rangle$ and $|2\rangle$.

When turning on the probe and signal fields, we can obtain the first and second order solutions of the system, respectively, and both are linear problems. We assume that the probe field (signal field) $\Omega_p^{(1)}$ ($\Omega_s^{(2)}$) is proportional to $e^{i\theta_p}$ ($e^{i\theta_s}$) with $\theta_p = K_p(\omega)x_0 - \omega t_0$ ($\theta_s = K_s(\omega)x_0 - \omega t_0$), which means $\Omega_p^{(1)} = F_1 e^{i(K_p(\omega)x_0 - \omega t_0)}$ ($\Omega_s^{(2)} = F_2 e^{i(K_s(\omega)x_0 - \omega t_0}$), where F_1 (F_2) are slowly varying envelop function of multiscale variables yet to be determined. Then, we can obtain the linear dispersion relations of the probe field and signal field interacting with the double EIT medium, which read

$$K_p(\omega) = \frac{\omega}{c} + \kappa_{14} \frac{(\omega + d_{31})\sigma_{11}^{(0)}}{D_p}, \quad (4a)$$

$$K_s(\omega) = \frac{1}{n_{\text{eff}}} \frac{\omega}{c} + \kappa_{24} \frac{(\omega + d_{32})\sigma_{22}^{(0)}}{D_s}, \quad (4b)$$

where ω is the frequency shift to the center frequency of the probe and signal fields, and we

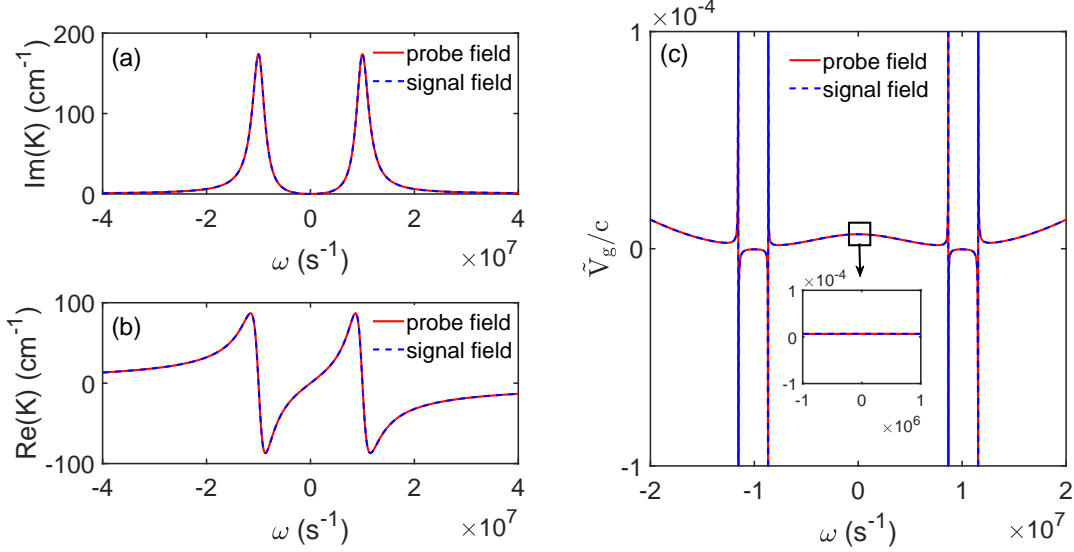


FIG. 2. The linear dispersion relations and group velocities of the probe field and signal fields. (a) The absorption spectrum $\text{Im}(K_{p(s)})$ and (b) the dispersion relation $\text{Re}(K_{p(s)})$ as functions of the frequency shift ω . (c) The group velocity \tilde{V}_g/c of the probe field and the signal field changes as functions of ω . The inset panel shows the group velocity matching region. The red solid line and blue dotted line correspond to the probe field and the signal field, respectively.

have defined $D_p = |\Omega_c|^2 - (\omega + d_{31})(\omega + d_{41})$ and $D_s = |\Omega_c|^2 - (\omega + d_{32})(\omega + d_{42})$.

$V_{g1} = \text{Re}[\partial K_p / \partial \omega]^{-1}$ and $V_{g2} = \text{Re}[\partial K_s / \partial \omega]^{-1}$ are the group velocities of probe field and signal field respectively. From Eqs. (4a) and (4b), we can find that the mainly difference of the linear dispersion relation K_p and K_s is induced by the parameters Δ_2 , κ_{j4} and Γ_{ij} ($i = 3, 4, j = 1, 2$), and the difference will cause the group velocities of the probe and signal field mismatch. In order to study the XPM between the probe and signal fields, the group velocities of the two fields must be well matched. Thus, in our following analyse, we choose these system parameters as $\Delta_2 = 0$, $\gamma_{13} = \gamma_{23}$ and $\gamma_{14} = \gamma_{24}$, which is a typical symmetrical double EIT scheme. Under this condition, the linear dispersion relations of probe field and signal field are almost the same, i.e., $K_p \approx K_s$, thus the group velocities are well matched as shown in Fig.2.

Figure 2 (a) and (b) show the imaginary part and real part of the linear dispersion relation $K_{p(s)}(\omega)$ as a function of the center frequency shift ω . The system parameters are chosen from the D1-line transition of ^{87}Rb atoms, with the energy levels selected as $|1\rangle =$

$|5^2S_{1/2}, F=1, m_F=-1\rangle$, $|2\rangle = |5^2S_{1/2}, F=2, m_F=1\rangle$, $|3\rangle = |5^2S_{1/2}, F=2, m_F=0\rangle$, and $|4\rangle = |5^2P_{1/2}, F=2, m_F=0\rangle$ [43]. The decay rates are given by $\Gamma_4 = 5.75$ MHz, $\Omega_c = 10$ MHz, $\Delta_2 = \Delta_3 = \Delta_4 = 0$, $\lambda_c = \lambda_p = \lambda_s = 780$ nm. The parameters of waveguide are $\mu_1 = 0.83+0.0001i$, $\mu_2 = 1$, $\varepsilon_1 = -31.14+0.32i$, $\varepsilon_2 = 1$, and $k(\omega_s) = k(\omega_p) = (8.17+0.0012i) \times 10^4$ cm⁻¹. The electric dipole matrix elements are $|\mathbf{p}_{14}| \simeq |\mathbf{p}_{24}| = 1.46 \times 10^{-27}$ C·cm. We assume that atomic density $\mathcal{N}_a \approx 1.10 \times 10^{11}$ cm⁻³, then $\kappa_{14} \approx \kappa_{24} \approx 1.0 \times 10^9$ cm⁻¹ s⁻¹. As shown in Fig. 2(a), we can see that the absorption doublet of the probe and signal fields are almost overlap under the double EIT effect, and as the dispersion properties shown in Fig. 2(b), which means the double EIT effect can hugely suppress the absorption of the two fields, and can satisfy the group velocity matching condition at the same time. In Fig. 2(c), the red solid line and blue dashed line represent the relationship between the group velocity \tilde{V}_g/c ($\tilde{V}_g = \text{Re}(V_g)$) and the frequency shift ω of the probe light field and the signal light field, respectively. We can see the group velocity of the signal field match the group velocity of the probe field well, and with a subluminal ($10^{-4}c$).

B. NONLINEAR PROPERTIES OF THE SYSTEM

In this subsection, we study the nonlinear excitation of SPs in this system. In the third and fourth order solution of the MB equations, we can obtain the solvable conditions, where the probe field and signal field envelope function F_1 and F_2 satisfies

$$i\left(\frac{\partial}{\partial x_2} + \frac{\partial}{\partial t_2} \frac{1}{V_{g1}}\right)F_1 + \frac{c}{2\omega_p} \frac{\partial^2}{\partial y_1^2} F_1 - W_{11}|F_1|^2 F_1 e^{-2\bar{\alpha}_1 x_2} = 0, \quad (5a)$$

$$i\left(\frac{\partial}{\partial x_2} + \frac{\partial}{\partial t_2} \frac{1}{V_{g2}}\right)e^{i\theta_s} F_2 + \frac{c}{2\omega_s n_{\text{eff}}} \frac{\partial^2}{\partial y_1^2} e^{i\theta_s} F_2 - W_{21}|F_1|^2 e^{i\theta_s} F_2 e^{-2\bar{\alpha}_1 x_2} = 0, \quad (5b)$$

with $\bar{\alpha} = \epsilon^{-2}\alpha_1 = \epsilon^{-2}\text{Im}[K_p(\omega)]$, W_{11} and W_{21} being the nonlinear coefficients describing self phase modulation (SPM) of the probe field and XPM between the probe and signal field, respectively. The relation between the nonlinear coefficients and the self-kerr and cross-kerr susceptibilities are

$$\chi_{11}^{(3)} = \frac{2c}{\omega_p} \frac{|\mathbf{p}_{14}|^2}{\hbar^2} W_{11}, \quad (6a)$$

$$\chi_{21}^{(3)} = \frac{2c}{\omega_s} \frac{|\mathbf{p}_{24}|^2}{\hbar^2} W_{21}. \quad (6b)$$

In general, the coefficients in Eq.(5) are complex, thus, the system does not allow stable local nonlinear solutions. Fortunately, if the system works under the condition of

double EIT, the imaginary part of these coefficients can be much smaller than the real part. In addition to the parameters mentioned above, we choose the other parameters as $\Omega_c = 1.0 \times 10^6$ Hz, $U_0 = 2.24 \times 10^8$ Hz, $R_y = 107$ nm, $\Delta_2 = 1.0 \times 10^4$ Hz, $\Delta_3 = 1.0 \times 10^5$ Hz and $\Delta_4 = 8.0 \times 10^7$ Hz. We can obtain that $W_{11} \approx (5.09 + 0.025i) \times 10^{-13} \text{cm}^{-1} \text{s}^2$, $W_{21} \approx (5.18 + 0.017i) \times 10^{-13} \text{cm}^{-1} \text{s}^2$. Based on Eq. (6), the self-kerr and cross-kerr susceptibilities $\chi_{11}^{(3)} = (2.42 + 0.012i) \times 10^{-2} \text{cm}^2 \text{V}^{-2}$, $\chi_{21}^{(3)} = (2.46 + 0.008i) \times 10^{-2} \text{cm}^2 \text{V}^{-2}$, respectively, which corresponding to giant Kerr effects. The typical diffraction length $L_{\text{Diff}} = \omega_{p(s)} R_y^2 / c$ of the system is approximately $9.24 \times 10^{-6} \text{cm}$, and the typical nonlinearity length $L_{\text{Nonl}} = 1/[U_0^2 \text{Re}(W_{11})]$ is approximately equal to L_{Diff} . Thus, the diffraction effect can balance the nonlinearity effect of the system. And then we have the linear absorption lengths $L_{\text{Ap(s)}} = 1/\text{Im}(K_{p(s)} + k_{p(s)})$ of the system, that are approximately $L_{\text{Ap}} = 0.0836 \text{ cm}$, $L_{\text{As}} = 0.0835 \text{ cm}$, we can get the condition $L_{\text{Ap(s)}} \gg L_{\text{Nonl}} \approx L_{\text{Diff}}$. R_y and $U_0 = 1/\sqrt{L_{\text{Diff}} \text{Re}(W_{11})}$ are radius in the transverse direction and typical half-Rabi frequency of the probe field, respectively. Under the above parameters condition, it is possible to obtain two-component soliton solutions of Eq.(5) [43].

C. Coupled NLSEs

For the convenience of research, we transform the Eq.(5a) and Eq.(5b) into dimensionless form, which are the coupled nonlinear Schrödinger equations (NLSEs), and the expressions are as following

$$i\left(\frac{\partial}{\partial s} + \frac{1}{\lambda_1} \frac{\partial}{\partial \tau}\right)u_1 + \frac{1}{2} \frac{\partial^2}{\partial \xi^2} u_1 - w_{11} u_1 |u_1|^2 = -iA_1 u_1, \quad (7a)$$

$$i\left(\frac{\partial}{\partial s} + \frac{1}{\lambda_2} \frac{\partial}{\partial \tau}\right)u_2 + \frac{1}{2} \frac{\partial^2}{\partial \xi^2} u_2 - w_{21} u_2 |u_1|^2 = -iA_2 u_2, \quad (7b)$$

where the dimensionless physical quantity are defined as $u_j = \epsilon F_j / U_0 e^{-\bar{\alpha}_j x_2}$, $s = x / L_{\text{Diff}}$, $\tau = t / \tau_0$, $\lambda_j = V_{gj} \tau_0 / L_{\text{Diff}}$, $\xi = y / R_y$, $w_{j1} = W_{j1} / |W_{11}|^2$ and $A_{1(2)} = L_{\text{Diff}} \alpha_{1(2)}$. And τ_0 is the pulse duration. To solve the above equation, we assume $u_j(\tau, s, \xi) = g_j(\tau, s) v_j(\tau, \xi)$ with

$$g_j(\tau, s) = \frac{1}{\sqrt[4]{4\pi\rho_0^2}} e^{-(s-\lambda_j\tau)^2/4\rho_0^2}, \quad (8)$$

where ρ_0 is a free real parameter. After neglecting the small absorption coefficient A_j and integrating the variable s , Eq.(7a) and Eq.(7b) are further simplified as

$$\left(\frac{i}{\lambda_1} \frac{\partial}{\partial \tau} + \frac{1}{2} \frac{\partial^2}{\partial \xi^2}\right) v_1 - \frac{1}{2\sqrt{\pi}\rho_0} w_{11} |v_1|^2 v_1 = 0, \quad (9a)$$

$$\left(\frac{i}{\lambda_2} \frac{\partial}{\partial \tau} + \frac{1}{2} \frac{\partial^2}{\partial \xi^2}\right) v_2 - \frac{1}{2\sqrt{\pi}\rho_0} w_{21} |v_1|^2 v_2 = 0. \quad (9b)$$

And then, we will study the spatial focusing effect of SPs based on the above equation.

IV. SPATIAL FOCUSING OF SPS BASED ON XPM

Eq. (9) has many soliton pair solutions[40], next, we choose three typical soliton pair solutions as the initial condition to study the XPM between the probe and signal fields, and spatial focusing of the signal field based on XPM.

(i) *Bright-bright soliton pair*. The expression of bright-bright soliton pair read

$$v_j = \varsigma_j \text{sech}[\varsigma_{jj}(\xi - \eta_j \tau - \xi_0)] e^{i[\eta_j \xi - (\eta_j^2 - \varsigma_j^2)\tau/2 - \varphi_0]}, \quad (j = 1, 2) \quad (10)$$

where ς_j , ς_{jj} , η_j , ξ_0 and φ_0 are free real parameters [43]. For numerical simulation, we

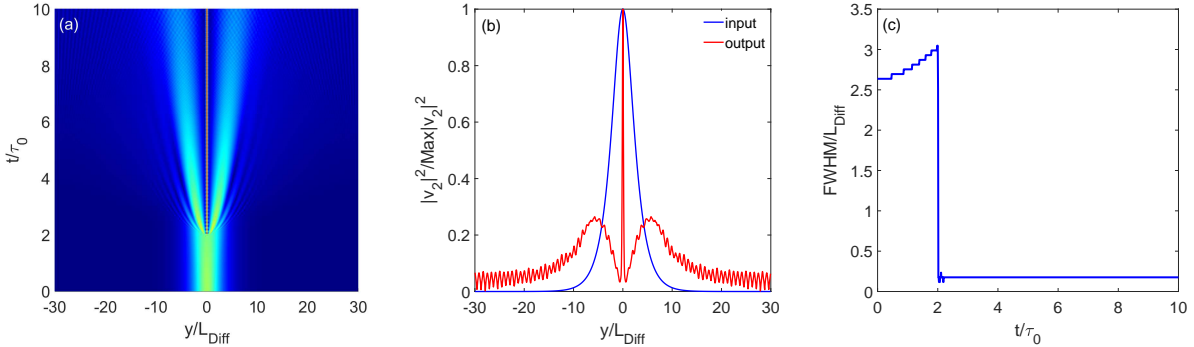


FIG. 3. (a) Time evolution of the bright SPs soliton v_2 . After the probe soliton v_1 is turned on at the position of $t/\tau_0 = 2$, v_2 will be obviously focused; (b) The input and output profile of the SPs soliton; (c) The FWHM of the SPs soliton changes with the propagation time t/τ_0 .

choose the following initial values of the free parameters as $\varsigma_1 = 8$, $\varsigma_2 = 1$, $\varsigma_{11} = 6$, $\varsigma_{22} = 0.6$, and the other are zeros.

In order to study the process of spatial focusing, we first input the SPs soliton v_2 , and then, turn on the probe soliton v_1 at the position of $t/\tau_0 = 2$. The results are shown in

Fig.3. We can see that the SPs soliton first undergoes a slight diffraction due to the absence of the term of XPM in Eq. (9b), when the narrow probe soliton is turned on, the SPs soliton is focused to a very tiny area in a very short response time, as shown in Fig.3(a). The physical mechanism of such effect is that the narrow probe soliton modulates the profile of the SPs soliton in the overlap area via XPM. We can see that the full width at the half-maximum (FWHM) of the output profile of the SPs soliton is much smaller than that of the input one from Fig.3(b). We also show the $\text{FWHM}/L_{\text{Diff}}$ as a function of the propagation time t/τ_0 in Fig.3(c). We can see that the FWHM of the initial SPs soliton is $2.2L_{\text{Diff}} \sim 203.28$ nm. After the spatial focusing, the curve dropped sharply, and the FWHM of the output SPs soliton is only $0.16L_{\text{Diff}} \sim 14.78$ nm, which is nearly 14 times compressed. Thus, even the nanofocusing of SPs can be realized in our scheme.

(ii) *Bright-bright soliton pairs.*

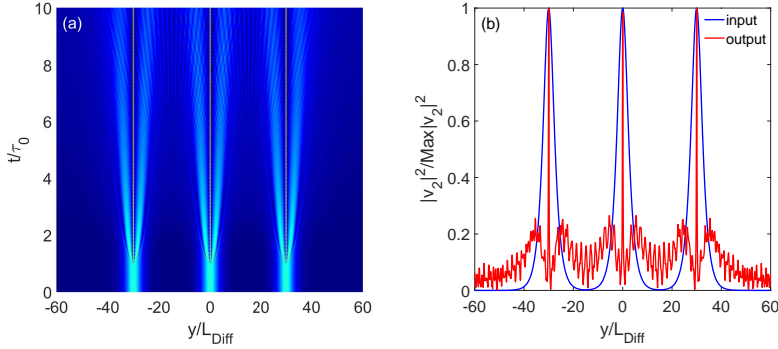


FIG. 4. (a) Time evolution of the multi SPs solitons v_2 . After the probe soliton v_1 is turned on at the position of $t/\tau_0 = 1$, v_2 will be obviously focused; (b) The input and output profile of the SPs solitons.

Eq. (9) also has multi soliton pairs solutions. Under the same condition as previous, we input three bright SPs solitons, and the initial positions are at $\xi_0 = -30, 0$ and 30 , respectively. And then we turn on the probe solitons with the same form of solution at $t/\tau_0 = 1$, as shown in Fig. 4(a). We find that such multi SPs solitons can also be focused with very narrow transverse width via XPM, the normalized input and output profiles are shown in Fig. 4(b). The FWHM of the input field is about $3.3L_{\text{Diff}}$. After the XPM, the pulse width of v_2 drops sharply and the output width is about $0.16L_{\text{Diff}}$, which is compressed nearly 20 times. Such results can be applied in the making of surface plasmon polaritons grating with high spectral resolution at micro/nano scale.

(iii) *Dark-dark soliton pair*. In order to verify the correctness of our theory, we also choose the dark solitons pair as the initial condition of our numerical simulation, the expressions of the dark solitons pair reads

$$v_j = \{\psi_j i \sin \phi_j + m_j \cos \phi_j \tanh[b_j(\xi - h\tau)]\} e^{in_j c_j \xi + i[c_j^2/2 + \chi_j]\tau}, (j = 1, 2), \quad (11)$$

where $\phi_j = \arctan[(c_j - b_j)/a_j]$, ψ_j , a_j , b_j , χ_j and c_j are real parameters [44]. The initial

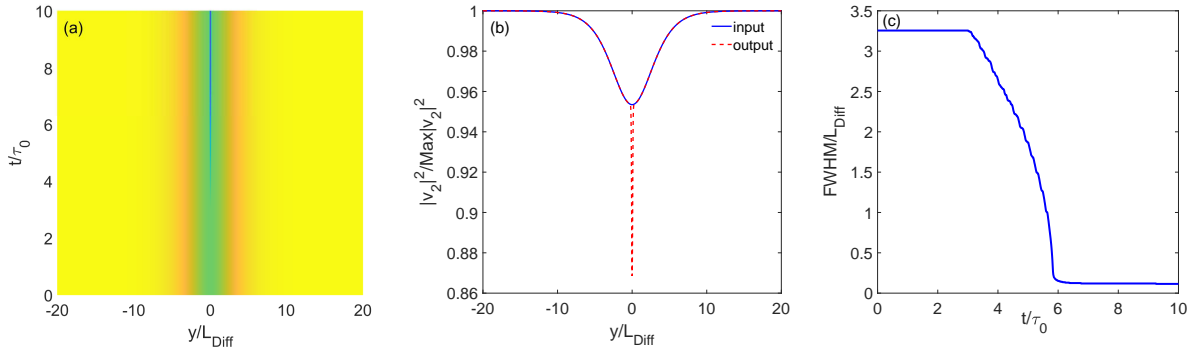


FIG. 5. (a) Time evolution of the dark SPs soliton v_2 . After the probe soliton v_1 is turned on at the position of $t/\tau_0 = 3$, v_2 will be obviously focused; (b) The input and output profile of the SPs soliton; (c) The FWHM of the SPs soliton changes with the propagation time t/τ_0 .

values of the free parameters are $\psi_1 = -8.14$, $a_1 = 3$, $b_1 = 18$, $c_1 = 2$, $m_1 = 6.51$, $n_1 = 0.4$, $\chi_1 = -2$, $\psi_2 = -1.20$, $a_2 = \sqrt{0.8}$, $b_2 = 0.3$, $c_2 = \sqrt{8}$, $m_2 = 1.07$, $n_2 = 0.28$, $\chi_2 = -4$, and the other parameters are zeros. The results are shown in Fig.5, and with some differences comparing to results obtained in the bright one. We can see that the SPs soliton first propagates stably when the XPM is absent, and when turn on the dark probe soliton at $t/\tau = 3$, a very narrow and deep dip appears in the overlap region between the signal and probe fields, *i.e.* spatial focusing, as shown in Fig. 5(a). In Fig. 5(b), we find that there are no higher harmonics beside the interacting region. The appearance of the narrow dip is due to the energy transfer in the XPM process. Shown in Fig. 5(c) is the $\text{FWHM}/L_{\text{Diff}}$ of the narrow dip as a function of t/τ_0 , we can see the FWHM of the SPs soliton drops slowly than that shown in Fig. 3(c), which means the interacting time between the dark soliton is longer than that of the bright soliton.

V. SUMMARY

In conclusion, a scheme based on XPM in double EIT is proposed to realize spatial focusing of SPs in a NIMM interface waveguide system. First, we obtain the low loss stable propagation of SPs, and the group velocities of the probe and signal fields are well matched under the double EIT condition in the linear region, and then, giant enhancement of the XPM can be obtained in the nonlinear region. Finally, the coupled NLSEs are derived in our system, by adopting the bright-bright soliton pair, multi bright solitons pairs and dark-dark soliton pair as the initial condition, we realize the spatial focusing of SPs solitons via XPM between the narrow optical soliton in free space and the SPs soliton, and even nanofocusing. We also find that the response time between the bright-bright soliton pair is much shorter than that of the dark one. These results not only provide a certain theoretical basis for realizing the active manipulation of SPs, but also have broad application prospects in the fields of micro-nano optics.

ACKNOWLEDGMENTS

This work was supported by National Natural Science Foundation of China (NSFC) under Grant Nos. 11604185, 11704066, 11804196 and 11947072.

APPENDIX

Appendix A: Expressions related to the electric field of SPs

The permittivity (ε_1) and the permeability (μ_1) of NIMM can be described by the Drude model, i.e., $\varepsilon_1(\omega_s) = \varepsilon_\infty - \omega_e^2/\omega_s(\omega_s + i\gamma_e)$, $\mu_1(\omega_s) = \mu_\infty - \omega_m^2/\omega_s(\omega_s + i\gamma_m)$, where $\omega_{e,m}$ are electric and magnetic plasma frequencies of the NIMM, $\gamma_{e,m}$ are corresponding decay rates, and ε_∞ and μ_∞ are background constants.

The decay coefficients along the z direction read $k_j^2 = k(\omega_s)^2 - \varepsilon_j\mu_j\omega_s^2/c^2$, where $j = 1$ for the NIMM, $j = 2$ for the atomic gas, and satisfies the relation $k_1\varepsilon_2 = -k_2\varepsilon_1$, which gives the propagation constant of the SPs, i.e., $k(\omega_s) = \omega_s[\varepsilon_1\varepsilon_2(\varepsilon_1\mu_2 - \varepsilon_2\mu_1)/(\varepsilon_1^2 - \varepsilon_2^2)]^{1/2}/c$. The electric field of SPs in the atomic gas reads $\mathbf{E}_s(\mathbf{r}, t) = \mathcal{E}_s(\mathbf{r}, t)\mathbf{u}_s(z) \exp[i(k(\omega_s)x - \omega_s t)] + c.c.$, with the mode function being $\mathbf{u}_s(z) = -c[k(\omega_s)\hat{\mathbf{z}} - ik_2(\omega_s)\hat{\mathbf{x}}]e^{k_2z}/\varepsilon_2\omega_s$. In our analysis, above

system parameters are given by $\varepsilon_\infty = 1$, $\mu_\infty = 1$, $\omega_e = 1.37 \times 10^{16} \text{ s}^{-1}$, $\omega_m = 2.45 \times 10^{15} \text{ s}^{-1}$, $\gamma_e = 2.73 \times 10^{13} \text{ s}^{-1}$ (as for Ag), and $\gamma_m = \gamma_e/1000$. For a detailed derivation, one can refer to Ref. [35].

Appendix B: Equations of motion for the density-matrix elements

The explicit Bloch equations describe the density matrix element σ_{jl} ($j, l = 1, 2, 3, 4$) under the interaction representation as follows:

$$i \frac{\partial}{\partial t} \sigma_{11} - i \Gamma_{14} \sigma_{44} + \Omega_p^* \sigma_{41} - \Omega_p \sigma_{41}^* = 0, \quad (\text{B1a})$$

$$i \frac{\partial}{\partial t} \sigma_{22} - i \Gamma_{24} \sigma_{44} + \zeta(z)^* e^{-i\theta_s^*} \Omega_s^* \sigma_{42} - \zeta(z) e^{-i\theta_s} \Omega_s \sigma_{42}^* = 0, \quad (\text{B1b})$$

$$i \frac{\partial}{\partial t} \sigma_{33} - i \Gamma_{34} \sigma_{44} + \Omega_c^* \sigma_{43} - \Omega_c \sigma_{43}^* = 0, \quad (\text{B1c})$$

$$i \left(\frac{\partial}{\partial t} + \Gamma_4 \right) \sigma_{44} + \Omega_p \sigma_{41}^* + \zeta(z) e^{i\theta_s} \Omega_s \sigma_{42}^* + \Omega_c \sigma_{43}^* - \Omega_p^* \sigma_{41} - \zeta(z)^* e^{-i\theta_s^*} \sigma_{42} - \Omega_c^* \sigma_{43} = 0, \quad (\text{B1d})$$

$$\left(i \frac{\partial}{\partial t} + d_{21} \right) \sigma_{21} + \zeta(z)^* e^{-i\theta_s^*} \Omega_s^* \sigma_{41} - \Omega_p \sigma_{42}^* = 0, \quad (\text{B1e})$$

$$\left(i \frac{\partial}{\partial t} + d_{31} \right) \sigma_{31} + \Omega_c^* \sigma_{41} - \Omega_p \sigma_{43}^* = 0, \quad (\text{B1f})$$

$$\left(i \frac{\partial}{\partial t} + d_{32} \right) \sigma_{32} + \Omega_c^* \sigma_{42} - \zeta(z) e^{i\theta_s} \Omega_s \sigma_{43}^* = 0, \quad (\text{B1g})$$

$$\left(i \frac{\partial}{\partial t} + d_{41} \right) \sigma_{41} + \Omega_p (\sigma_{11} - \sigma_{44}) + \zeta(z) e^{i\theta_s} \Omega_s \sigma_{21} + \Omega_c \sigma_{31} = 0, \quad (\text{B1h})$$

$$\left(i \frac{\partial}{\partial t} + d_{42} \right) \sigma_{42} + \zeta(z) e^{i\theta_s} \Omega_s (\sigma_{22} - \sigma_{44}) + \Omega_p \sigma_{21}^* + \Omega_c \sigma_{32} = 0, \quad (\text{B1i})$$

$$\left(i \frac{\partial}{\partial t} + d_{43} \right) \sigma_{43} + \Omega_c (\sigma_{33} - \sigma_{44}) + \Omega_p \sigma_{31}^* + \zeta(z) e^{i\theta_s} \Omega_s \sigma_{32}^* = 0, \quad (\text{B1j})$$

where $d_{jl} = \Delta_j - \Delta_l + i\gamma_{jl}$ ($j, l = 1, 2, 3, 4$), the decoherence rate of change of the system is defined as $\gamma_{jl} = (\Gamma_j + \Gamma_l)/2$, where $\Gamma_j = \sum_{E_i < E_j} \Gamma_{ij}$.

Appendix C: Solutions of the asymptotic expansion at the first and second orders

1. First-order approximation

$$\Omega_p^{(1)} = F_1 e^{i\theta_1} = F_1 e^{i[K_p(\omega)x_0 - \omega t_0]}, \quad (\text{C1a})$$

$$\sigma_{31}^{(1)} = -\frac{\Omega_c^* \sigma_{11}^{(0)}}{D_p} F_1 e^{i\theta_1}, \quad (\text{C1b})$$

$$\sigma_{41}^{(1)} = \frac{(\omega + d_{31})\sigma_{11}^{(0)}}{D_p} F_1 e^{i\theta_1}. \quad (\text{C1c})$$

The solution of other density matrix elements is zero, where $D_p = |\Omega_c|^2 - (\omega + d_{31})(\omega + d_{41})$ and $\theta_1 = K_p(\omega)x_0 - \omega t_0$ are defined. F_1 is the pending envelope function of the probe field, which is related to the slow variables y_1 , t_2 and x_2 .

2. Second-order approximation

$$\Omega_s^{(2)} = F_2 e^{i\theta_2} = F_2 e^{i[K_s(\omega)x_0 - \omega t_0]}, \quad (\text{C2a})$$

$$\sigma_{11}^{(2)} = a_{11}^{(2)} |F_1|^2 e^{-2\alpha_1 x_2}, \quad (\text{C2b})$$

$$\sigma_{22}^{(2)} = a_{22}^{(2)} |F_1|^2 e^{-2\alpha_1 x_2}, \quad (\text{C2c})$$

$$\sigma_{32}^{(2)} = a_{32}^{(2)} \zeta_s(z) e^{i\theta_s} F_2 e^{i\theta_2}, \quad (\text{C2d})$$

$$\sigma_{33}^{(2)} = a_{33}^{(2)} |F_1|^2 e^{-2\alpha_1 x_2}, \quad (\text{C2e})$$

$$\sigma_{42}^{(2)} = a_{42}^{(2)} \zeta_s(z) e^{i\theta_s} F_2 e^{i\theta_2}. \quad (\text{C2f})$$

We define $D_s = |\Omega_c|^2 - (\omega + d_{32})(\omega + d_{42})$ and $\theta_2 = K_s(\omega)x_0 - \omega t_0$. F_2 is the envelope function of the signal light field to be determined and related to the slow variables y_1 , t_2

and x_2 , and the coefficient $a_{jl}^{(2)}$ in the formula is:

$$a_{11}^{(2)} = -\frac{\sigma_{11}^{(0)}}{2D_p^*}, \quad (\text{C3a})$$

$$a_{22}^{(2)} = -\frac{\sigma_{11}^{(0)}}{2D_p^*}, \quad (\text{C3b})$$

$$a_{32}^{(2)} = -\frac{\Omega_c^* \sigma_{22}^{(0)}}{D_s}, \quad (\text{C3c})$$

$$a_{33}^{(2)} = -\frac{\sigma_{11}^{(0)}}{D_p^*}, \quad (\text{C3d})$$

$$a_{42}^{(2)} = -\frac{(\omega + d_{32})\sigma_{22}^{(0)}}{D_s}. \quad (\text{C3e})$$

3. Third-order approximation

$$\sigma_{41}^{(3)} = i \frac{\partial}{\partial t_2} \frac{[|\Omega_c|^2 + (\omega + d_{31})^2] \sigma_{11}^{(0)}}{D_p^2} \Omega_p^{(1)} + \frac{(\omega + d_{31}) a_{11}^{(2)}}{D_p} |\Omega_p^{(1)}|^2 \Omega_p^{(1)}. \quad (\text{C4})$$

The explicit expression of the SPM coefficient W_{11} in Eq. (5a) reads

$$W_{11} = -\kappa_{14} \frac{(\omega + d_{31}) a_{11}^{(2)}}{D_p} = \kappa_{14} \frac{(\omega + d_{31}) \sigma_{11}^{(0)}}{2|D_p|^2}. \quad (\text{C5})$$

4. Fourth-order approximation

The explicit expression of the XPM coefficient W_{21} in Eq. (5b) reads

$$W_{21} = -\kappa_{24} \frac{(\omega + d_{32}) a_{22}^{(2)}}{D_s} = \kappa_{24} \frac{(\omega + d_{32}) \sigma_{11}^{(0)}}{2D_s D_p^*}. \quad (\text{C6})$$

-
- [1] P. Groß, M. Esmann, S. F. Becker, J. Vogelsang, N. Talebi, and C. Lienau, Plasmonic nanofocusing - grey holes for light, *Adv. Phys. : X* **1**, 297 (2016).
 - [2] P. Dombi, Z. Pápa, J. Vogelsang, S. V. Yalunin, M. Sivilis, G. Herink, S. Schäfer, P. Groß, C. Ropers, and C. Lienau, Strong-field nano-optics, *Rev. Mod. Phys.* **92**, 025003 (2020).
 - [3] C. C. Neacsu, S. Berweger, R. L. Olmon, L. V. Saraf, C. Ropers, and M. B. Raschke, Near-Field Localization in Plasmonic Superfocusing: A Nanoemitter on a Tip, *Nano. Lett.* **10**, 592 (2010).

- [4] D. Sadiq, J. Shirdel, J. S. Lee, E. Selishcheva, N. Park, and C. Lienau, Adiabatic Nanofocusing Scattering-Type Optical Nanoscopy of Individual Gold Nanoparticles, *Nano. Lett.* **11**, 1609 (2011)
- [5] S. Schmidt, B. Piglosiewicz, D. Sadiq, J. Shirdel, J. S. Lee, P. Vasa, N. Park, D. S. Kim, and C. Lienau, Adiabatic Nanofocusing on Ultrasmooth Single-Crystalline Gold Tapers Creates a 10-nm-Sized Light Source with Few-Cycle Time Resolution, *ACS Nano.* **6**, 6040 (2012).
- [6] F. Huth, M. Schnell, J. Wittborn, N. Ocelic, and R. Hillenbrand, Infrared-spectroscopic nanoimaging with a thermal source, *Nat. Mater.* **10**, 352 (2011).
- [7] R. Zhang, Y. Zhang, Z. C. Dong, S. Jiang, C. Zhang, L. Chen, L. Zhang, Y. Liao, J. Aizpurua, Y. Luo, J. Yang, and J. Hou, Chemical mapping of a single molecule by plasmon-enhanced Raman scattering, *Nature* **498**, 82 (2013).
- [8] J. Zhong, X. Jin, L. Meng, X. Wang, H. Su, Z. Yang, C. T. Williams, and B. Ren, Probing the electronic and catalytic properties of a bimetallic surface with 3 nm resolution, *Nat. Nanotechnol.* **12**, 132 (2017).
- [9] M. Liu, F. Lu, W. Zhang, L. Huang, S. Liang, D. Mao, F. Gao, T. Mei, and J. Zhao, Highly efficient plasmonic nanofocusing on a metallized fiber tip with internal illumination of the radial vector mode using an acousto-optic coupling approach, *Nanophotonics* **8**, 921 (2019).
- [10] L. Zhu, Y. Yin, L. Dai, Y. Hu, J. Nan, Z. Zheng, C. Cai, W. Zhao, and M. Ding, Round-tower plasmonic optical microfiber tip for nanofocusing with a high field enhancement, *Opt. Commun.* **453**, 124358 (2019).
- [11] F. Lu, W. Zhang, L. Zhang, M. Liu, T. Xue, L. Huang, F. Gao, and T. Mei, Nanofocusing of Surface Plasmon Polaritons on Metal-Coated Fiber Tip Under Internal Excitation of Radial Vector Beam, *Plasmonics* **14**, 1593 (2019).
- [12] T. Umakoshi, M. Tanaka, Y. Saito, and P. Verma, White nanolight source for optical nanoimaging, *Sci. Adv.* **6**, 4179 (2020).
- [13] M. Esmanna, A. Chimeha, A. Korte, J. Zhong, S. Stephan, J. Wittb, G. Wittstock, N. Talebi, and C. Lienau, Plasmonic nanofocusing spectral interferometry, *Nanophotonics* **9**, 491 (2020).
- [14] R. C. Dunn, Near-field scanning optical microscopy, *Chem. Rev.* **99**, 2891 (1999).
- [15] J. N. Anker, W. P. Hall, O. Lyadres, N. C. Shah, J. Zhao, and R. P. V. Duyne, Biosensing with plasmonic nanosensors, *Nat. Mater.* **7**, 308 (2009).

- [16] R. M. Stockle, Y. D. Suh, V. Deckert, and R. Zenobi, Nanoscale chemical analysis by tip-enhanced Raman spectroscopy. *Chem. Phys. Lett.* **318**, 131 (2000).
- [17] S. Berweger, J. M. Atkin, R. L. Olmon, and M.B. Raschke, Adiabatic tip-plasmon focusing for nano-Raman spectroscopy, *J. Phys. Chem. Lett.* **1**, 3427 (2010).
- [18] A. W. Bargioni, A. Schwartzberg, M. Cornaglia, A. Ismach, J. J. Urban, Y. Pang, R. Gordon, J. Bokor, M. B. Salmeron, D. F. Ogletree, P. Ashby, and S. Cabrini, P. J. Schuck, Hyper-spectral nanoscale imaging on dielectric substrates with coaxial optical antenna scan probes, *Nano. Lett.* **4**, 1201 (2011).
- [19] J. Stadler, T. Schmid, and R. Zenobi, Developments in and practical guidelines for tip-enhanced Raman spectroscopy, *Nanoscale* **4**, 1856 (2012).
- [20] C. Chen, N. Hayazawa, and S. Kawata, A 1.7 nm resolution chemical analysis of carbon nanotubes by tip-enhanced Raman imaging in the ambient, *Nat. Commun.* **5**, 3312 (2014).
- [21] F. Lu, T. Huang, L. Han, H. Su, H. Wang, M. Liu, W. Zhang, X. Wang, and T. Mei, Tip-enhanced Raman spectroscopy with high-order fiber vector beam excitation, *Sensors* **18**, 3841 (2018).
- [22] W. Zhang, C. Li, K. Gao, F. Lu, M. Liu, X. Li, L. Zhang, D. Mao, F. Gao, L. Huang, T. Mei, and J. Zhao, Surface-enhanced Raman spectroscopy with Au-nanoparticle substrate fabricated by using femtosecond pulse, *Nanotechnolo.* **29**, 205301 (2018).
- [23] C. C. Neacsu, G. A. Reider, and M. B. Raschke, Second-harmonic generation from nanoscopic metal tips: symmetry selection rules for single asymmetric nanostructures, *Phys. Rev. B* **71**, 201402(R) (2005).
- [24] M. Kauranen, and A. V. Zayats, Nonlinear plasmonics, *Nat. Photonics* **6**, 737 (2012).
- [25] V. Kravtsov, R. Ulbricht, J. M. Atkin, and M. B. Raschke, Plasmonic nanofocused four-wave mixing for femtosecond near-field imaging, *Nat. Nanotechnolo.* **11**, 459 (2016).
- [26] S. Keramati, A. Passian, V. Khullar, and H. Batelaan, Photofield electron emission from an optical fiber nanotip, *Appl. Phys. Lett.* **117**, 061102 (2020).
- [27] R. Zia, J. A. Schuller, and M. L. Brongersma, Near-field characterization of guided polariton propagation and cutoff in surface plasmon waveguides, *Phys. Rev. B* **74**, 165415 (2006).
- [28] E. Verhagen, L. Kuipers, and A. Polman, Enhanced Nonlinear Optical Effects with a Tapered Plasmonic Waveguide, *Nano. Lett.* **7**, 334 (2007).

- [29] H. Choo, M. K. Kim, M. Staffaroni, T. J. Seok, J. Bokor, S. Cabrini, P. J. Schuck, M. C. Wu, and E. Yablonovitch, Nanofocusing in a metal-insulator-metal gap plasmon waveguide with a three-dimensional linear taper, *Nat. Photonics* **6**, 838 (2012).
- [30] V. A. Zenin, A. Andryieuski, R. Malureanu, I. P. Radko, V. S. Volkov, D. K. Gramotnev, A. V. Lavrinenko, and S. I. Bozhevolnyi, Boosting Local Field Enhancement by on-Chip Nanofocusing and Impedance-Matched Plasmonic Antennas, *Nano. Lett.* **15**, 8148 (2015).
- [31] P. Li, D. Pan, L. Yang, H. Wei, S. He, H. Xu, and Z. Li, Silver nano-needles: focused optical field induced solution synthesis and application in remote excitation nanofocusing SERS, *Nanoscale* **11**, 2153 (2019).
- [32] A. Kamli, S. A. Moiseev, and B. C. Sanders, Coherent Control of Low Loss Surface Polaritons, *Phys. Rev. Lett.* **101**, 263601 (2008).
- [33] S. Asgarneshad-Zorgabad, R. Sadighi-Bonabi, and B. C. Sanders, Excitation and propagation of surface polaritonic rogue waves and breathers, *Phys. Rev. A* **98**, 013825 (2018).
- [34] S. Asgarneshad-Zorgabad, P. Berini, and B. C. Sanders, Polaritonic frequency-comb generation and breather propagation in a negative-index metamaterial with a cold four-level atomic medium, *Phys. Rev. A* **99**, 051802(R) (2019).
- [35] Q. Liu, N. Li, and C. Tan, All-Optical Logic Gate Based on Manipulation of Surface Polaritons Solitons via External Gradient Magnetic Fields, *Phys. Rev. A* **101**, 023818 (2020).
- [36] G. P. Agrawal, Amplification of Ultrashort Solitons in Erbium-Doped Fiber Amplifiers, *IEEE Photonics Technol. Lett.* **2**, 875 (1990).
- [37] G. P. Agrawal, *Nonlinear Fiber Optics* (Sixth Edition) (Academic press, 2019).
- [38] X. Liu, Dynamic evolution of temporal dissipative-soliton molecules in large normal path-averaged dispersion fiber lasers, *Phys. Rev. A* **82**, 063834 (2010).
- [39] X. Liu, Soliton formation and evolution in passively-mode-locked lasers with ultralong anomalous-dispersion fibers, *Phys. Rev. A* **84**, 023835 (2011).
- [40] Y. S. Kivshar, G. P. Agrawal, *Optical solitons: from fibers to photonic crystals* (Academic press, 2003).
- [41] G. Huang, L. Deng, and M. G. Payne, Dynamics of ultraslow optical solitons in a cold three-state atomic system, *Phys. Rev. E* **72**, 016617 (2005).
- [42] Z. Chen, M. Segev, T. H. Coskun, D. N. Christodoulides, Y. S. Kivshar, Coupled photorefractive spatial-soliton pairs, *J. Opt. Soc. Am. B* **14**, 3066 (1997).

- [43] Z. Chen, H. Xie, Q. Li, and G. Huang, Stern-Gerlach deflection of optical Thirring solitons in a coherent atomic system, *Phys. Rev. A* **100**, 013827 (2019).
- [44] A. P. Sheppard, and Y. S. Kivshar, Polarized dark solitons in isotropic Kerr media, *Phy. Rev. E* **55**, (1997).